CHEMISTRY

Acceptorless dehydrogenation and hydrogenation of N- and O-containing compounds on $Pd_3Au_1(111)$ facets

Xinjiang Cui[1], Zhangjun Huang[1], Antoine P. van Muyden[1], Zhaofu Fei[1], Tao Wang[2]*, Paul J. Dyson[1]*

Catalytic dehydrogenation and hydrogenation of amines and alcohols are important in the synthesis of fine chemicals. Despite several efficient homogeneous catalysts having been identified, highly active heterogeneous catalysts remain elusive, although they would meet an unmet need. Here, we show that bimetallic Pd-Au nanoparticles with Pd-to-Au molar ratios of 3:1 immobilized on multiwall carbon nanotubes (Pd_3Au_1/CNT) display high catalytic activity in the oxidant-free and acceptorless dehydrogenation and hydrogenation of N- and O-containing heterocyclic compounds, amines/imines, and alcohols/ketones. Transmission electron microscopy analysis demonstrates the preferential exposure of $Pd_3Au_1(111)$ facets on the Pd_3Au_1/CNT catalyst. Mechanistic insights combining experimental data with density functional theory calculations reveal that the $Pd_3Au_1(111)$ surface enhances both dehydrogenation and hydrogenation reactions and provides a rationale for the observed enhancements.

INTRODUCTION

Catalytic hydrogenation and, to a lesser extent, dehydrogenation reactions are extensively used in the preparation of a wide and diverse range of chemicals, ranging from simple fuels to complex pharmaceutical products (*1*, *2*). For example, N- and O-containing compounds such as indoles, quinolines, ketones, and their hydrogenated derivatives may be prepared via catalytic hydrogenation and dehydrogenation reactions (*3*, *4*). In addition to affording valuable chemical products, reversible catalytic dehydrogenation and hydrogenation of N- and O-containing compounds could potentially lead to practical hydrogen carriers (*2*, *5*, *6*). The introduction of nitrogen or oxygen atoms is considered advantageous for this latter application as they decrease the endothermicity of the dehydrogenation reaction lower than that of hydrocarbons (*7*).

Dehydrogenation and hydrogenation reactions involving homogeneous catalysts are well developed, although most catalyze either the hydrogenation reaction or the opposite dehydrogenation (*7*–*12*). However, catalysts able to both dehydrogenate and hydrogenate N- and O-containing compounds are becoming increasingly attractive, and well-defined molecular catalysts based on Ir (*10*, *11*, *13*), Ru (*14*), Co (*15*), and Fe (*7*) have been reported. A recent prominent example comprises homogeneous Ir complexes with substituted triazolylidene ligands that catalyze the reversible, acceptorless dehydrogenation of 1,2,3,4-tetrahydroquinoline to quinoline in water (*13*). The dehydrogenation and hydrogenation of various heterocycles has also been achieved with visible-light photoredox catalysts and electrocatalysts based on homogeneous Co (*15*) and Fe (*16*) complexes.

Despite the excellent performance of these homogeneous catalysts on a laboratory scale, their large-scale implementation is limited by their high cost, stability, and complex recycling protocols. In this respect, heterogeneous catalysts have intrinsic advantages that overcome these limitations, and a number of promising catalysts have been developed (*17*). However, previous systems required either high catalyst loadings or high temperatures to achieve high efficiency, and the substrate scope was mostly limited to several amines (*18*). Recently, a Co single-atom catalyst was shown to catalyze the dehydrogenation of N-heterocycles to release H_2 and the transfer hydrogenation of N-heterocycles using formic acid as a hydrogen source to afford formamides (*19*). However, subsequent dehydrogenation of the formamides is problematic and prevented reversible hydrogenation/dehydrogenation cycles. Heterogeneous catalysts that efficiently catalyze both dehydrogenation and hydrogenation of N- and O-containing compounds remain elusive. Notably, limited information is available on the catalytically active sites and the reaction mechanism of heterogeneous catalysis.

Bimetallic catalysts combining Pd and Au are known to be highly active for the oxidative activation of carbon-hydrogen bonds in alcohols, toluene, and methane (*20*–*22*) and in hydrogenation reactions (*23*). However, Pd-Au nanoparticles have not been studied in the acceptorless dehydrogenation of amines and alcohols and the reverse hydrogenation reactions. With the inspiration by these improvements, we report on the discovery of a multiwall carbon nanotube (CNT)–stabilized Pd-Au bimetallic nanoparticle (NP) system that preferentially exposes $Pd_3Au_1(111)$ facets and displays high catalytic activity in the acceptorless dehydrogenation and reverse hydrogenation of N-heterocycles, amines/imines, and alcohols/ketones. Mechanistic studies were performed, and the high catalytic activity was investigated by DFT calculations, which shows that the $Pd_3Au_1(111)$ surface lowers energy barriers in each of the elementary steps in both reactions.

RESULTS

Catalyst preparation and characterization

A series of Pd-Au bimetallic NPs using trisodium citrate dihydrate (TCD) as stabilizing reagent to prevent the aggregation of the NPs and immobilized on CNTs were prepared from aqueous solutions of K_2PdCl_4 (0.02 M) and $HAuCl_4$ (0.015 M) by varying the Pd:Au ratio to generate a series of materials containing a total metal content of 2 weight % (wt %). The CNTs were dispersed in water containing TCD (with a metal:TCD ratio of 1:3), to which the aqueous solutions

[1]Institute of Chemical Sciences and Engineering, École Polytechnique Fedérale de Lausanne (EPFL), CH-1015, Lausanne, Switzerland. [2]SUNCAT Center for Interface Science and Catalysis, Department of Chemical Engineering, Stanford University, Stanford, CA 94305, USA.
*Corresponding author. Email: paul.dyson@epfl.ch (P.J.D.); twang86@stanford.edu (T.W.)

containing the metal precursors were added dropwise. The resulting suspensions were heated to 30°C for 30 min, excess $NaBH_4$ was subsequently added, and the mixture was maintained at 30°C for 2 hours to afford powders. The powders were filtered, washed with water, and dried under vacuum (see Materials and Methods for full synthetic details). Catalysts with Pd-to-Au molar ratios of 3:1 (Pd_3Au_1/CNT), 1:1 (Pd_1Au_1/CNT), and 1:3 (Pd_1Au_1/CNT) were prepared together with monometallic Pd (Pd/CNT) and Au (Au/CNT) systems as controls. The metal ratios and loadings were measured by an inductively coupled plasma optical emission spectrometer(ICP-OES).

Transmission electron microscopy (TEM) and high-angle annular dark-field scanning transmission electron microscopy (HAADF-STEM) were used to characterize the catalysts [see Fig. 1 (A to C) for the Pd_3Au_1 catalyst and figs. S1 and S2 for the other catalysts]. The Pd_3Au_1 NPs are uniformly dispersed on the CNTs in the Pd_3Au_1/CNT catalyst with the NPs having a narrow size distribution of 2 to 4 nm with an average diameter of 2.48 ± 0.22 nm (Fig. 1A and fig. S1A). Figure 1B shows the high-resolution TEM (HRTEM) image of a typical Pd-Au bimetallic NP with an interplanar spacing of 2.3 Å, which corresponds to a face-centered cubic (fcc) lattice structure with a (111) surface (*21*). HAADF-STEM was used to investigate the elemental distribution of the Pd-Au NPs. Figure 1F shows the HAADF-STEM crossline profile of the sample shown in Fig. 1C (corresponding to the red line). The overlap of the Pd and Au profiles demonstrates the coexistence of both metals in the NP and is indicative of local alloying. HAADF-STEM–energy dispersive spectroscopy (EDS) mapping for the Pd_3Au_1/CNT catalyst (Fig. 1, D and E) corroborates the notion of a Pd-Au alloy. Moreover, HAADF-STEM images of the catalysts with different metal ratios have similar mean particle sizes, ranging from 2.32 ± 0.12 nm to 2.89 ± 0.16 nm, and with similar particle size distributions. Moreover, there is no clear correlation between size and catalytic activity, and since the sizes are similar, the difference in catalytic activities observed cannot be attributed to differences between the size of the NPs (figs. S1 and S2). The size of the Pd_3Au_1 NPs increases to 2.64 ± 0.25 nm after dehydrogenation (compared to 2.48 nm in the pristine catalyst). Because of the apparent stability of the catalyst in hydrogenation and dehydrogenation reactions, we assumed that the small change in particle size does not strongly affect the catalytic activity (fig. S2).

X-ray diffraction (XRD) pattern of the Au/CNT catalyst (Fig. 1G) exhibits crystalline features corresponding to Au(111) and Au(200). The Au(111) diffraction peak is slightly shifted from 38.34 ± 0.03 eV in the Au/CNT material to 38.56 ± 0.03 eV in the Pd_3Au_1/CNT catalyst, further supporting an alloy structure with the (111) facet

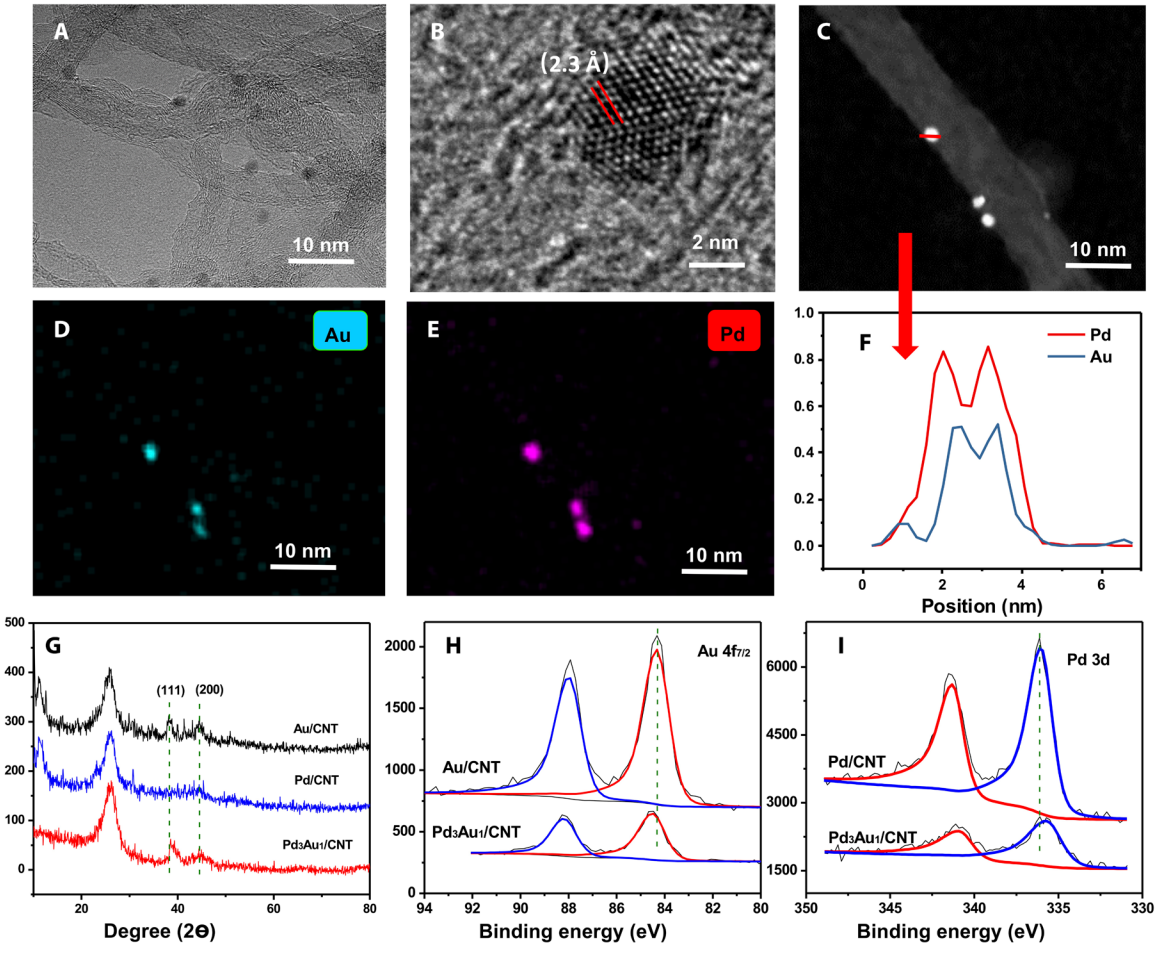

Fig. 1. Characterization of the Pd_3Au_1/CNT catalyst. (**A**) Bright-field TEM image; (**B**) HRTEM image; (**C**) HAADF-STEM image. HAADF-TEM-EDS mapping images of the Pd_3Au_1/CNT catalyst: (**D**) Au; (**E**) Pd; (**F**) crossline profiles of elemental composition for the Pd-Au NP. (**G**) XRD patterns of the Au/CNT, Pd/CNT, and Pd_3Au_1/CNT catalysts. XPS of (**H**) Au 4f spectra of the Au/CNT and Pd_3Au_1/CNT catalysts and (**I**) Pd 3d spectra of the Pd/CNT and Pd_3Au_1/CNT catalysts.

exposed preferentially. Note that larger Au NPs are formed at high Au loadings (figs. S1 and S2). The electronic structures of the supported NPs with different Pd:Au ratios were probed with x-ray photoelectron spectroscopy (XPS). In the Pd_3Au_1/CNT catalyst, the peaks located at 84.48 ± 0.02 eV and 88.15 ± 0.02 eV (Fig. 1H) may be attributed to Au 4f, and the peaks located at 335.69 and 340.96 eV correspond to Pd 3d (Fig. 1I), and confirm the presence of metallic Au^0 and Pd^0 in an alloy structure. The binding energies (BEs) of Pd 3d in Pd_3Au_1/CNT shift to lower values compared to the Pd 3d BE in Pd/CNT (Pd $3d_{5/2}$, 336.08 ± 0.02 eV; Pd $3d_{3/2}$, 341.29 ± 0.02 eV), while the Au 4f BEs in Pd_3Au_1/CNT move to higher values related to the Au 4f BE in Au/CNT (Au $4f_{7/2}$, 84.32 ± 0.02 eV; Au $4f_{5/2}$, 87.99 ± 0.02 eV). This change indicated the alloying of Pd-Au NPs and the electronic modification of Pd with Au. XPS analysis of the Pd_3Au_1/CNT catalyst reveals a Pd:Au ratio of 3.2:1 with the Pd predominantly in the metallic state, consistent with Pd-Au alloys immobilized on carbon and TiO_2 surfaces (*21*). Furthermore, the O 1s and C 1s signals are similar for both the Pd_3Au_1/CNT and CNT materials, and sodium is not observed on the Pd_3Au_1/CNT, indicating that TCD is not retained on the surface of the catalyst. This is confirmed by ^1H and ^{13}C nuclear magnetic resonance (NMR) spectroscopy of the filtrate of the catalyst after ultrasonication in D_2O. After 5 cycles, the BEs of the Pd_3Au_1/CNT catalyst for Pd $3d_{5/2}$ and Au $4f_{7/2}$ are 335.76 ± 0.01 eV and 84.39 ± 0.01 eV (fig. S3), respectively, which are similar to the BEs of the fresh catalyst, confirming the stability of the bimetallic catalyst.

Catalytic dehydrogenation and hydrogenation studies

The catalytic dehydrogenation of 1,2,3,4-tetrahydro-quinoline (**1a**) was chosen as the benchmark reaction to determine the optimum catalyst and conditions under oxidant-free and acceptorless conditions. Xylene was used as a solvent as it should be inert under the reaction conditions used. The monometallic Pd/CNT and Au/CNT catalysts afford the dehydrogenated product in only 30 and 8% yields, respectively (table S1, entries 2 and 3). In contrast, the bimetallic catalysts are considerably more active; the Pd_3Au_1/CNT catalyst, by heating in xylene at 140°C for 12 hours using 0.3 mole percent (mol %) of metals relative to **1a**, displays the highest activity with quinoline (**2a**) obtained in 96% yield (table S1, entry 4) with 321 of TON (turnover number; moles of product per mole of Pd and Au) and 26.8 of TOF (turnover frequency; TON/reaction time). Under the optimal conditions, the Pd_3Au_1/CNT catalyst is also superior to commercial catalysts (table S1, entries 7 and 8) and various homogeneous Pd catalysts (table S1, entries 9 to 12). Changing the solvents and reaction time did not improve the activity (table S1, entries 13 to 15). Moreover, the Pd_1Au_1 NPs supported on charcoal and Al_2O_3 showed lower yields on this dehydrogenation (table S1, entries 16 and 17).

The reverse reaction, i.e., the hydrogenation of quinoline, was studied under 1 bar of hydrogen. The reaction did not proceed in the presence of the Au/CNT catalyst (table S2, entry 1), whereas full conversion was achieved using the Pd/CNT catalyst, but the selectivity of reaction was low owing to the over-hydrogenation of quinoline to decahydroquinoline (table S2, entry 2). The bimetallic Pd_3Au_1/CNT catalyst resulted in the near-quantitative formation of tetrahydroquinoline by heating the mixture in xylene at 80°C and 1 bar H_2 for 12 hours using 0.3 mol % of metals relative to **2a** (table S2, entry 3) without conversion for xylene, whereas the Pd_1Au_1/CNT and Pd_1Au_3/CNT catalysts were both less active and selective (table S2, entries 4 and 5), and yields were reduced under more ambient conditions (table S2, entries 6 and 7). In addition, using Pd_3Au_1/C and Pd_3Au_1/Al_2O_3, **2a** was hydrogenated to **1a** with 71 and 84% yields, respectively.

Following removal of the Pd_3Au_1/CNT catalyst from the reaction (hot filtration test), reactivity was suppressed, implying that the active sites in heterogeneous CNT-supported Pd_3Au_1 NPs might be stable and absent in the filtrate (fig. S4A for the dehydrogenation). In addition, a mercury poisoning experiment (*24*) was performed, with mercury reducing the yield of **2a** to only 10%. The lower yield obtained in the presence of mercury further indicates that the active catalyst corresponds to the Pd_3Au_1(111) NPs. The stability and recyclability of the Pd_3Au_1/CNT catalyst were also established, with continuous switching between hydrogenation and dehydrogenation modes. After each step, the Pd_3Au_1/CNT catalyst was recovered by centrifugation, and the product was quantified. The reversible catalytic transformation between **1a** and **2a** could be repeated multiple times with high catalytic activity retained (fig. S4B).

Dehydrogenation of N-heterocycles

The Pd_3Au_1/CNT catalyst was evaluated in the dehydrogenation of various N-heterocyclic compounds and displayed outstanding activity. As shown in Table 1, functional groups at the 2-, 3-, and 4-positions influenced the dehydrogenation reaction with the yield increasing (up to 95%) with the distance of the substituent from the N atom (Table 1, entries 2 to 4). Quinolines with CH_3, OH, F, or NH_2 groups at the 6- and 8-positions on the aromatic ring were transformed in 73 to 96% yields (Table 1, entries 5 to 8). N-heteroarenes such as 9,10-dihydroacridine, 5,6-dihydrophenanthridine, and 1,2,3,4-tetrahydrobenzo[h]quinoline were dehydrogenated selectively, and in all cases, the desired products were obtained in good to excellent yields (Table 1, entries 9 to 11). Hydroxyl-, methoxy-, and methyl carboxylate–substituted indolines were transformed under the optimized conditions in yields of 91 to 99% (Table 1, entries 14 to 18), confirming the high selectivity/tolerance of the catalyst.

Dehydrogenation of N-alkylated amines

Imines and amines are key intermediates in the synthesis of fine chemicals, pharmaceuticals, and natural products (*25*), obtained from condensation reactions of amines with active carbonyl compounds and self-coupling of primary amines (*26*, *27*). Imines can also be obtained from the oxidation of amines, and the dehydrogenation of amines to imines is particularly attractive as fewer side products tend to be generated (*28*). Thus, the Pd_3Au_1/CNT catalyst was evaluated in the dehydrogenation of N-alkylated amines to imines under the optimized conditions and was found to selectively provide the desired imines in high yields (Table 2, entries 1 and 2). Notably, substituted *N*-phenylbenzylamines with different substituent groups were converted to their respective imines in excellent yields (Table 2, entries 3 to 6). Moreover, *N*-alkyl substrates were successfully dehydrogenated to their corresponding imines in moderate yields (Table 2, entries 7 and 8). These imine/amine couples can be considered as liquid organic hydrogen carriers but with lower hydrogen storage capacities than heterocycles (*28*).

Dehydrogenation of amines and alcohols

The acceptorless dehydrogenation of primary amines to imines by heterogeneous catalysts provides an opportunity to produce imines

Table 1. Dehydrogenation of N-heterocycle derivatives using the Pd_3Au_1/CNT catalyst. Reaction conditions: Pd_3Au_1/CNT (0.3 mol % of metals to substrate), N-heterocyclic substrate (0.2 mmol), xylene (1 ml), N_2 atmosphere, and 140°C. *Isolated yield.

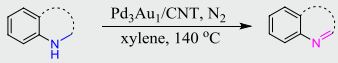

1a - 1q 2a - 2q

Entry	Substrate	Product	Time	Yield (%)*
1	(1a)	(2a)	12	96
2	(1b)	(2b)	20	74
3	(1c)	(2c)	15	87
4	(1d)	(2d)	15	95
5	(1e)	(2e)	12	96
6	(1f)	(2f)	20	73
7	(1g)	(2g)	20	96
8	(1h)	(2h)	12	93
9	(1i)	(2i)	20	96
10	(1j)	(2j)	20	89
11	(1k)	(2k)	15	89
12	(1l)	(2l)	6	99
13	(1m)	(2m)	12	94
14	(1n)	(2n)	6	99
15	(1o)	(2o)	12	92
16	(1p)	(2p)	12	93
17	(1q)	(2q)	12	96
18	(1r)	(2r)	12	91

and molecular hydrogen (*29*). The Pd_3Au_1/CNT serves as an efficient catalyst for the acceptorless dehydrogenation of primary amines under oxidant-free and base-independent conditions. Using the same reaction conditions used in the dehydrogenation of secondary amines, benzylamine was converted to the corresponding imine in 94% yield (table S3, entry 1). Nitrile formation was not detected (fig. S4E) (*30*), suggesting that the transamination step is much faster than the second dehydrogenation of the aldimine, which differs from the reactivity observed for homogeneous catalysts (*31*). Other substituted benzylamines with methyl and methoxy groups were efficiently and selectively dehydrogenated to the desired products (table S3, entries 2 to 4). 2-Picolylamine was transformed into the corresponding imine in 93% yield (table S3, entry 5), and an aliphatic amine afforded the dehydrogenated imine in 64% yield

Table 2. Dehydrogenation of N-alkylated amines using the Pd_3Au_1/CNT catalyst. Reaction conditions: Pd_3Au_1/CNT (0.3 mol % of metals to substrate), N-alkylated amine (0.2 mmol), xylene (1 ml), N_2 atmosphere, 140°C, and 24 hours. *Isolated yield. †NMR yields with diphenylmethanol as standard.

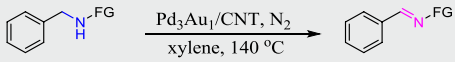

Entry	Substrate	Product	Yields (%)*
1	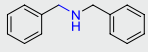 (**3a**)	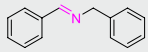 (**4a**)	93
2	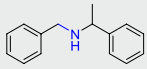 (**3b**)	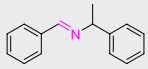 (**4b**)	89
3	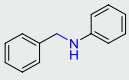 (**3c**)	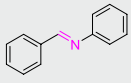 (**4c**)	92
4	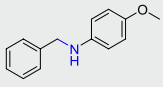 (**3d**)	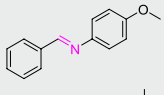 (**4d**)	98
5	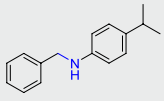 (**3e**)	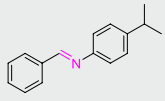 (**4e**)	98
6	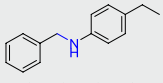 (**3f**)	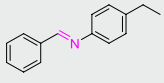 (**4f**)	87
7	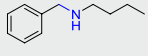 (**3g**)	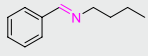 (**4g**)	79†
8	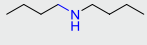 (**3h**)	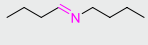 (**4h**)	52†

without the formation of a nitrile or N-alkylated amine (table S3, entry 6). In the presence of the Pd_3Au_1/CNT catalyst, imines are selectively obtained, which may be attributed to the combination of the two metals. Pd is very active for hydrogenations, whereas Au is much less active, and when alloyed, the Pd_3Au_1 facet has the ideal electronic properties to dehydrogenate the amine but not further hydrogenate the imine to alkylating amines.

The catalytic dehydrogenation of alcohols represents an attractive route to aldehydes and ketones that can be further transformed into imines, amides, esters, carboxylic acids, and various heterocycles (*3*, *32*). Consequently, we evaluated the Pd_3Au_1/CNT catalyst in the acceptorless dehydrogenation of alcohols. Secondary benzylic alcohols were successfully dehydrogenated to their corresponding acetophenone derivatives in excellent yields (table S3, entries 7 and 8). Moreover, diphenylmethanol was converted to the corresponding product in 98% yield (table S3, entry 9), and 1-indanol and 1,2,3,4-tetrahydro-1-naphthol react much faster with high yields after 12 hours as the ring systems facilitate catalytic dehydrogenation (table S3, entries 10 and 11).

Catalytic hydrogenation of N-heterocycles, imines, and ketones

Catalytic hydrogenation of a range of N- and O-containing compounds was studied using the Pd_3Au_1/CNT catalyst under the optimized conditions. As shown in Table 3, quinoline derivatives with electron-donating (–OH and $–NH_2$) and electron-withdrawing (–F) substituents were converted in high yields to the corresponding hydrogenated derivatives (Table 3, **1a** to **1h**). Methyl groups on different positions of the quinoline framework appeared to have little impact on the catalytic hydrogenation (Table 3, **1b** and **1c**). N-heteroarenes such as 9,10-dihydroacridine and 1,2,3,4-tetrahydrobenzo[h]quinoline were obtained in 87 and 88% yields, respectively (Table 3, **1i** and **1k**). In addition, quinoxaline and isoquinoline were hydrogenated in near-quantitative yields to the expected products (Table 3, **1l** and **1m**), whereas the hydrogenation of indole derivatives required a higher hydrogen pressure of 5 bars to achieve high yields, presumably due to their highly resonance-stabilized aromatic structure (Table 3, **1n** and **1r**). The activity displayed by the Pd_3Au_1/CNT catalyst is superior to other heterogeneous catalysts that tend to require harsher reaction conditions, which lowers selectivity (*17*).

Prompted by the promising results obtained with N-heterocycles, we investigated the hydrogenation of imines and carbonyls. The imine hydrogenation reactions were performed in toluene at 80°C under 1 bar of H_2 in the presence of the Pd_3Au_1/CNT catalyst. Dibenzylamine and *N*-benzyl-α-methylbenzylamine were obtained following the hydrogenation of the corresponding imines (Table 3, **3a** and **3b**, respectively). *N*-benzylideneaniline, 4-methoxy-*N*-benzylideneaniline, 4-isopropyl-*N*-benzylideneaniline, and 4-ethyl-*N*-benzylideneaniline were efficiently reduced within 12 hours to afford their corresponding *N*-benzylanilines in excellent yields (Table 3, **3c** to **3f**). However, debenzylation takes place, lowering the yield (71 to 86%) of the desired products. The Pd_3Au_1/CNT catalyst also catalyzes the

Table 3. Hydrogenation of unsaturated N-heterocycles, imines, and ketones. Reaction conditions: Pd_3Au_1/CNT (0.3 mol % of metals to substrate), substrate (0.2 mmol), xylene (0.5 ml), 80°C, H_2 (1 bar), and 12 hours. Isolated yield. *H_2 (5 bar). †Toluene.

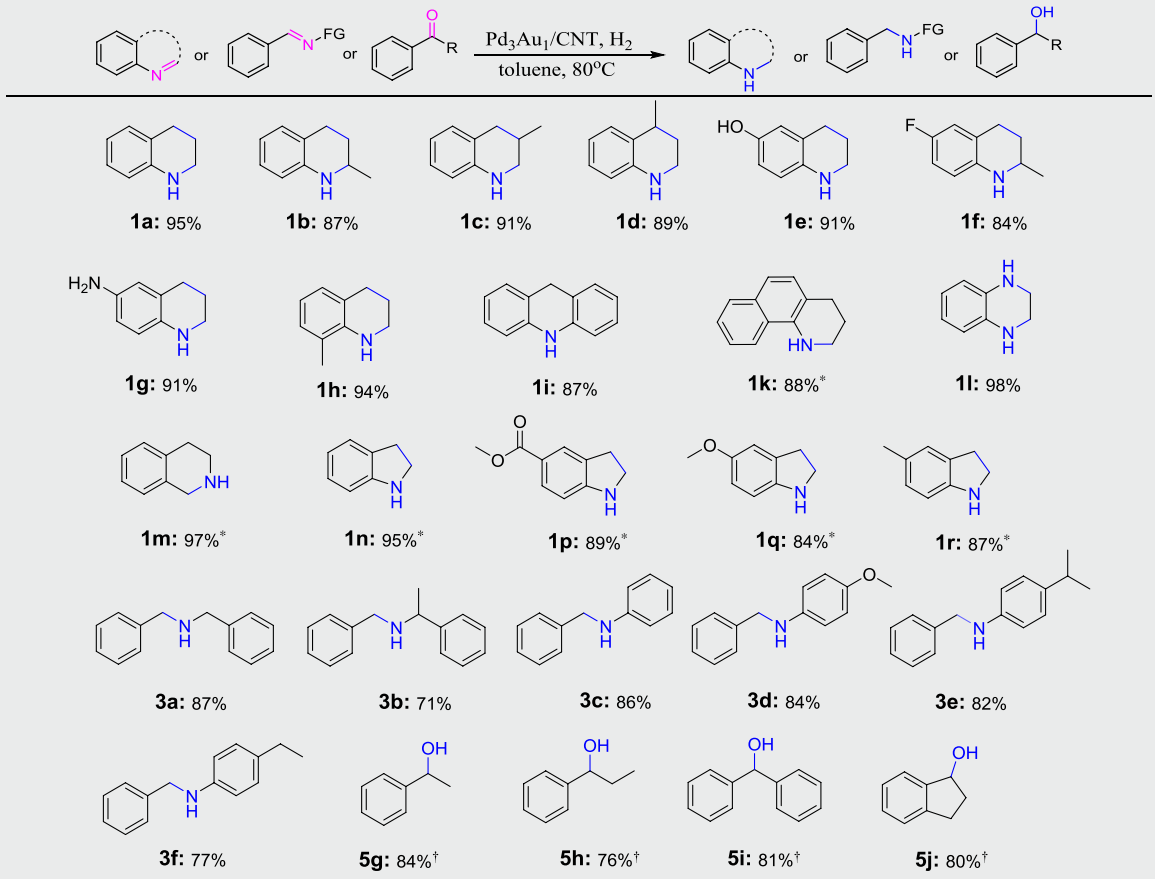

hydrogenation of carbonyls to their corresponding alcohols, demonstrated by the synthesis of 1-phenylethanol, 1-phenyl-1-propanol, benzhydrol, and 1-hydroxyindan from their ketone precursors (Table 3, **5g** to **5j**).

DISCUSSION

Control experiments and mechanistic studies

A tentative mechanism for the dehydrogenation and hydrogenation reaction, i.e., interconversion between **1a** and **2a**, using the Pd_3Au_1/CNT catalyst is illustrated in Fig. 2A. For the dehydrogenation reaction, **1a** is adsorbed on the $Pd_3Au_1(111)$ surface (**I** in Fig. 2A), activating the N—H and C—H bonds and leading to the liberation of the first H_2 and the formation of intermediate **1a**″ (**II** in Fig. 2A). Next, the intermediate in **1a**″ undergoes tautomerization to afford **2a**″. A second dehydrogenation step takes place, involving the same N—H and C—H bonds, to complete the process with the release of the second H_2 and the formation of **2a** (**III** in Fig. 2A and fig. S4F).

To substantiate the proposed mechanism, a number of control experiments were performed. No conversion was observed under dehydrogenation conditions using 1,2,3,4-tetrahydronaphthalene, 1-methyl-1,2,3,4-tetrahydroquinoline, or 2,2,4,7-tetramethyl-1,2,3,4-tetrahydroquinoline as the starting materials (Fig. 2B). These experiments all indicated that a N—H bond is essential for the reaction to proceed and indirectly supports the tautomerization step. Isomerization of C=N to C=C appears to be rapid, as **1a**″ was not observed and the dehydrogenation of 1,2-dihydroquinoline (**2a**″) was very fast (fig. S4C). The dehydrogenation of indoline-d_2, used as a model compound, was studied in situ by ^{1}H NMR spectroscopy, confirming that the tautomerization step as indoline-d_2 was quantitatively converted to indole with 20% of the N-D product resulting from the tautomerization process (Fig. 2C and scheme S2). Moreover, the formation of HD was also observed (*33*).

To further understand the differences in catalytic performance between the Pd and Pd_3Au_1 NP catalysts, DFT calculations were carried out. The (111) surface of both catalysts was chosen for all

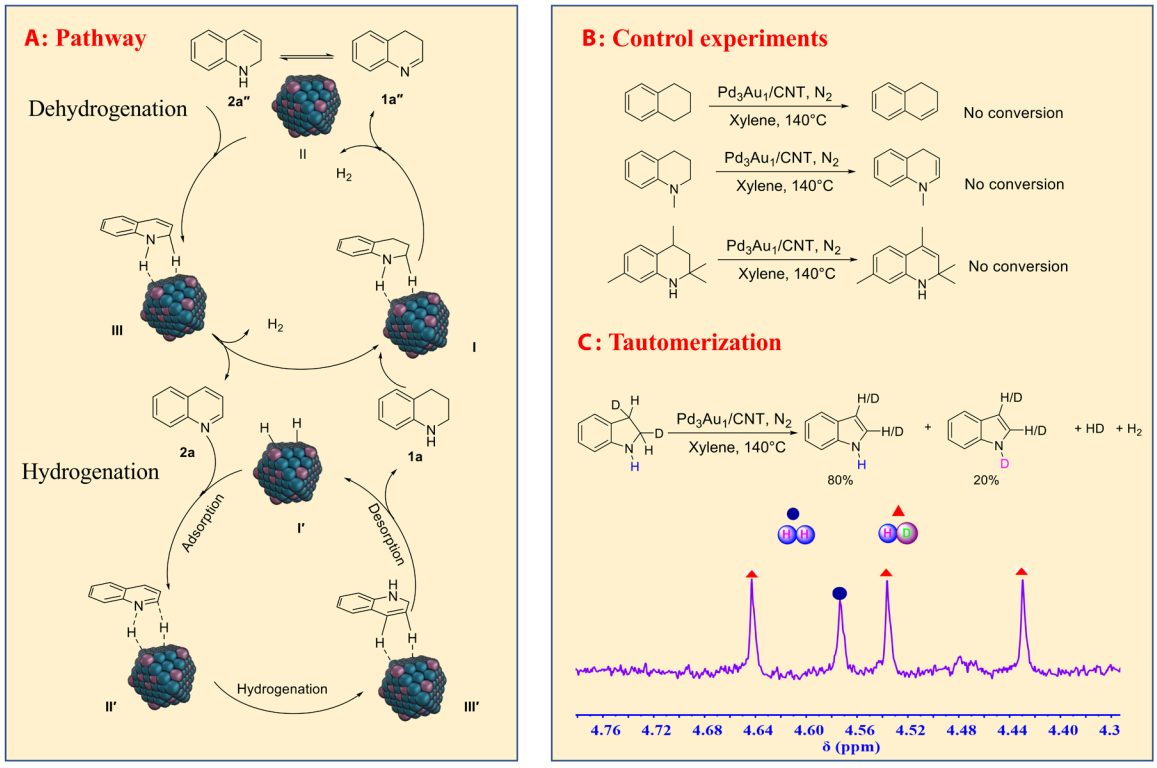

Fig. 2. Mechanism studies. (**A**) Proposed mechanism of the dehydrogenation and hydrogenation cycles. (**B**) Control experiments for the dehydrogenation. (**C**) Tautomerization study under conditions: Pd_3Au_1/CNT (0.3 mol % of metals to **1a**), **1a** (0.2 mmol), xylene (1 ml), N_2 atmosphere, and 140°C.

simulations as the structural data strongly suggest that it is the main facet orientation [Fig. 1 (B and G) for Pd_3Au_1 and fig. S2A for Pd]. The mechanism for the hydrogenation of quinoline involves sequential addition of H to the nitrogen and carbon atoms of quinoline. However, there are several possibilities for the first H addition, i.e., to the N atoms or to the C atoms of quinoline. We therefore calculated the energy barriers of the first H addition to N and the different C atoms and found that the formation of the N—H bond is the most favorable pathway with the lowest energy barrier. Next, for the addition of the second H to the partially hydrogenated quinoline, we calculated the energy barriers for H addition on the C atoms, allowing the most favorable pathway for the second H addition to be identified. Following this procedure, we identified the most favorable pathway for the hydrogenation. Other potential pathways include ring opening via C—C bond scission, which was not considered in this work because no such products were detected experimentally.

Figure 3A depicts the potential-free energy diagrams for the dehydrogenation of **1a** at 140°C. The $Pd_3Au_1(111)$ surface leads to lower-energy barriers for each dehydrogenation step compared to the Pd(111) facet. The energy barriers of the four dehydrogenation steps are 0.91, 0.57, 0.85, and 0.25 eV on $Pd_3Au_1(111)$ compared to values of 1.15, 0.92, 1.07, and 0.36 eV on the Pd(111) surface. Here, the energetic span model (*34*) was applied to compare the differences in activity of the two catalysts, which provides an elegant way to evaluate the TOF for a reaction. In this model, only one transition state, i.e., the TOF-determining transition state (TDTS), and one intermediate, i.e., the TOF-determining intermediate (TDI), determine the TOF in catalytic cycles. The TDTS-TDI energy difference and the reaction driving force (ΔGr) define the energetic span (δE) of the reaction, and a lower δE indicates higher activity. On the basis of the Gibbs free energy diagram in Fig. 3A, the δE values for the dehydrogenation of **1a** on the $Pd_3Au_1(111)$ and Pd(111) surfaces are 2.04 and 2.69 eV, respectively. This indicates the superior activity of the Pd_3Au_1 catalyst in dehydrogenation reactions, which is in line with the experimental data.

In addition, the reaction mechanisms for the selective hydrogenation of **2a** to **1a** on the Pd_3Au_1 (111) and Pd(111) surfaces were also calculated, and the associated free energy profile is shown in Fig. 3B. As expected, initial hydrogenation takes place at the C═N bond to afford intermediate **2a**′, which is subsequently converted to **2a**″. The energy barrier for the hydrogenation of the C═C in **2a**″ is much lower than that of the C═N bond in **2a**, and in a control experiment, it was shown that **2a**″ is quantitatively hydrogenated to **1a** in 3 hours (fig. S4D). Notably, the $Pd_3Au_1(111)$ surface leads to lower-energy barriers than those observed on the Pd(111) surface for each of the elementary step, due to modulation of the electronic properties of the active Pd atoms by the Au atoms and the CNT surface. Furthermore, the δE values for the hydrogenation of **2a** to **1a** on $Pd_3Au_1(111)$ and Pd(111) surfaces are 1.59 and 1.63 eV, respectively. This indicates the better activity of Pd_3Au_1 compared to the Pd catalyst in this hydrogenation reaction. To better understand the differences in selectivity of these two catalysts, we further calculated the reaction mechanism for the further hydrogenation of aromatic ring in **1a**. As shown in the potential-free diagram (fig. S5), the δE values for hydrogenation of aromatic ring of **1a** to $\mathbf{1a}^{4H}$ on the $Pd_3Au_1(111)$ and Pd(111) surfaces are 1.58 and 1.45 eV, respectively, which shows that Pd is more active in the hydrogenation

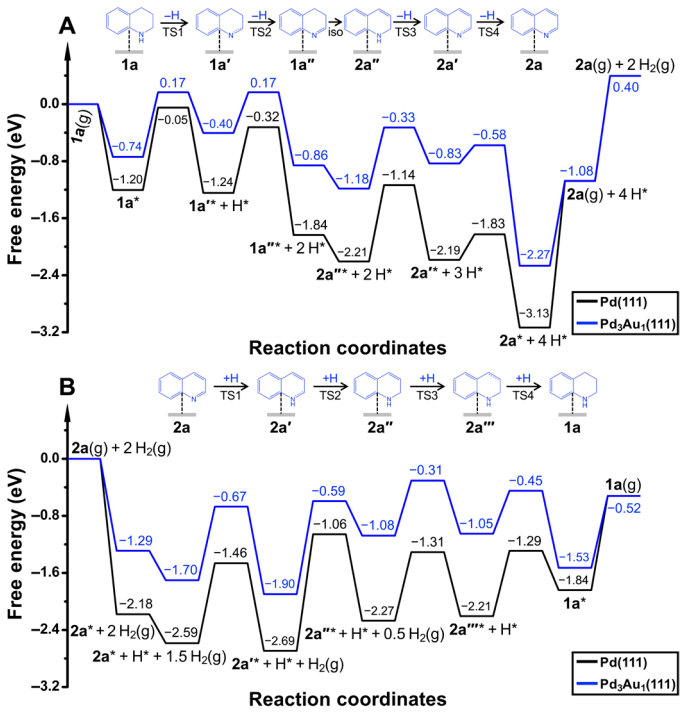

Fig. 3. Potential-free energy diagrams. (**A**) Dehydrogenation of **1a** at 140°C and (B) hydrogenation of **2a** at 80°C on the Pd(111) and Pd_3Au_1(111) surfaces.

of aromatic ring than the Pd_3Au_1 catalyst. In this respect, the calculations indicate that the Pd_3Au_1 catalyst has higher activity and selectivity for the selective hydrogenation of **2a** to **1a**, whereas the Pd(111) catalyst tends to over-hydrogenate the product, lowering the selectivity to **1a**. All these results are in good agreement with our experimental findings.

To establish the origin of the superior performance of the Pd_3Au_1 catalyst compared to the Pd_1Au_1, Pd_1Au_3, Pd, and Au systems, we considered the Sabatier principle (*35*), in which the interactions between the adsorbate and catalyst should be neither too strong nor too weak but ideally poised to activate the substrate and release the product. As shown in Fig. 3A, the adsorption of quinoline (**2a***) corresponds to the TDI of this reaction, which also indicates its important role in determining the performance of the catalysts. We therefore chose the adsorption energy of **2a** as the descriptor to compare the intrinsic differences among the catalysts. As shown in table S4, Pd(111) and Au(111) have the strongest (−3.03 eV) and weakest (−0.91 eV) adsorption energies for **2a**, indicating their less promising performance in dehydrogenation reactions based on the Sabatier principle. However, the adsorption energy of **2a** in the Pd_3Au_1(111) surface is −2.14 eV, stronger than that of Pd_1Au_1(111), Pd_1Au_3(111), and Au(111) but weaker than that of Pd(111). Combined with the catalytic performance, the Pd_3Au_1(111) displays optimal adsorption energies of **2a**, leading to the superior performance of this catalyst. In this respect, the reason for the superior performance of Pd_3Au_1(111) to other Pd-Au–based catalysts could be attributed to its optimal adsorption strengths of adsorbates as intrinsically driven by the Sabatier principle.

In summary, we described the development of a highly efficient bimetallic Pd_3Au_1/CNT catalyst for the dehydrogenation and hydrogenation of N- and O-containing compounds. The mechanism of the interconversion between 1,2,3,4-tetrahydroquinoline and quinoline was probed as a model reaction using experimental methods and consolidated by DFT calculations, which show that the Pd_3Au_1(111) facet leads to lower-energy barriers than those observed on the Pd(111) surface for all of the elementary steps in both dehydrogenation and hydrogenation reactions. The high selectivity of the Pd_3Au_1/CNT catalyst allows it to be used in the synthesis of a wide range of N- and O-containing compounds offering a practical strategy for the synthesis of N-heterocycles, amines/imines, and alcohols/ketones substrates, tolerating a wide range of functional groups via dehydrogenation and hydrogenation reactions, in the absence of additives.

MATERIALS AND METHODS

Preparation of the Pd_3Au_1/CNT catalyst

First, multiwalled CNTs were pretreated under 10 M HNO_3 for 12 hours at 80°C. After purification treatment, the Fe and Co content in the CNT was 0.04 and 0.01 wt %, respectively, and other metals such as Ni, Cr, and Pt are lower than the limit of detection of ICP-OES. CNT (200 mg) was added to an aqueous solution (10 ml) containing $HAuCl_4{\cdot}3H_2O$ (3.14 mg/0.008 mmol) and K_2PdCl_4 (7.77 mg/0.024 mmol, Pd:Au molar ratio of 3:1). Under vigorous stirring (~700 rpm), an aqueous solution (10 ml) containing TCD (28.2 mg/0.096 mmol, 3 eq relative to the metals) was added. The solution was stirred for 30 min at 30°C and $NaBH_4$ (6.08 mg/0.16 mmol) was added, and the mixture was maintained at 30°C for 2 hours. The resulting black powder was filtered and washed with distilled water to reach a pH value of 7. After drying under vacuum for 12 hours, the catalyst was stored under N_2 and used for the dehydrogenation and hydrogenation without further treatment.

Preparation of the Pd_1Au_1/CNT, Pd_1Au_3/CNT, Pd/CNT, and Au/CNT catalyst

These catalysts were prepared using a similar procedure to the one mentioned above, but the amount of the Pd and Au was changed, affording 2.0 wt % of metals.

General procedure for dehydrogenation reactions

Pd_3Au_1/CNT (5 mg), starting material (0.2 mmol), and xylene (1.5 ml) were placed in an oven-dried Schlenk tube and charged with nitrogen three times. The sealed Schlenk tube was heated to 140°C for 24 hours. After reaction, the flask was cooled to room temperature, and the reaction mixture was diluted using ethyl acetate and analyzed by gas chromatography–mass spectrometry (GC-MS) or NMR spectroscopy. To isolate the products, the volatiles were removed under vacuum, and the residues were further purified by column chromatography. All the dehydrogenated products were characterized by NMR spectroscopy in $CDCl_3$ (see fig. S6 for ^1H and ^{13}C NMR of **1a** and **2a**).

General procedure of hydrogenation reactions

Pd_3Au_1/CNT (5 mg), starting material (0.2 mmol), and xylene or toluene (1.5 ml) were added to a 25-ml stainless steel pressure reactor. The reactor was sealed, flushed three times with H_2, and placed under an appropriate H_2 pressure (1 to 5 bar). The mixture was heated to 80°C and stirred for 12 hours. After reaction, the reactor was cooled to room temperature, and the solution was diluted with ethyl acetate. After analysis by GC and GC-MS, the mixture was filtered through a silica gel column, and the volatiles were removed under

vacuum. The residues were further purified by column chromatography. All the dehydrogenated products were characterized by NMR spectroscopy in $CDCl_3$.

Computational details

DFT computations were carried out using the plane wave–based method as implemented in the Vienna ab initio simulation package (*36*). Periodic slab models were used to simulate the Pd and Pd-Au alloy catalysts. The projector augmented wave (*37*) method was applied to describe the electron-ion interaction, and the electron exchange and correlation energy were treated within the generalized gradient approximation in the Perdew-Burke-Ernzerhof formalism. To obtain accurate energies with errors less than 1 meV per atom, a cutoff energy of 400 eV was chosen for all computations. A second-order Methfessel-Paxton electron smearing with $\sigma = 0.2$ eV was used. Structure optimization was performed when the force tolerance and energy difference became <0.02 eV/Å and 10^{-5} eV, respectively. A vacuum layer of 15 Å was set between the periodically repeating slabs to avoid strong interactions. The density-dependent dDsC method was used for the dispersion correction (*38*). To elucidate the intrinsic differences of the Pd and Pd-Au systems in hydro-treating reactions, we chose fcc Pd and Pd_3Au_1 for further reaction mechanism investigations and comparisons. Computations of the fcc-bulk Pd and Pd_3Au_1 crystal structures with a *k*-point mesh of $19 \times 19 \times 19$ give lattice constants of 3.91 and 3.96 Å, respectively. The most stable close-packed (111) surfaces of these two catalysts as confirmed by the surface energy (J/m^2) calculations [Pd(100), 1.53; Pd(110), 1.57; Pd(111), 1.34; Pd(210), 1.63; Pd(211), 1.61; Pd(310), 1.63; Pd(321), 1.59; Pd_3Au_1(100), 1.04; Pd_3Au_1(110), 1.33; Pd_3Au_1(111), 1.02; Pd_3Au_1(210), 1.48; Pd_3Au_1(211), 1.28; Pd_3Au_1(310), 1.47; Pd_3Au_1(321), 1.42] were applied for reaction mechanism simulations, where extensive model tests were performed to validate our choices of models. To have a balance between the computational accuracy and cost, a $p(4 \times 4)$-3L supercell was eventually used to simulate the Pd(111) and Pd_3Au_1(111) surfaces (fig. S5), and the first layer was fully relaxed, while the bottom two layers were constrained. In addition, *k*-point mesh for sampling the Brillouin zone was also tested, and a $(3 \times 3 \times 1)$ *k*-point mesh is accurate enough to acquire converged adsorption energies. Regarding the free energies in this work, the hydrogenation of quinoline in gas phase was used to benchmark the method for thermal corrections to gas phase species. We noticed that the results within ideal gas approximation were in very good agreement with experimental results (i.e., −1.29 eV[theory] versus −1.24 eV[experiment] for changes in reaction enthalpy at 298K). Therefore, the ideal gas approximation was applied to evaluate the free energies of gas phase species. The harmonic approximation as implemented in the Atomic Simulation Environment python library (*39*) was used to describe the thermodynamic corrections for adsorbates.

The adsorption energies of surface species were defined as $E_{ads} = E_{(adsorbate/surface)} - E_{(surface)} - E_{(adsorbate)}$, where $E_{(adsorbate/surface)}$, $E_{(surface)}$, and $E_{(adsorbate)}$ are the total electronic energies of species adsorbed on the Pd(111) and Pd_3Au_1(111) surfaces, clean surfaces, and species in the gas phase, respectively. The climbing image nudged elastic band method was used to locate transition-state structures of each primary step (*40*). The energy barrier (E_a) is defined as $E_a = E_{TS} - E_{IS}$, and the reaction energy is defined as $E_r = E_{FS} - E_{IS}$, where E_{IS}, E_{FS}, and E_{TS} are the total energies of the initial state (IS), final state (FS), and transition state (TS) of each elementary step, respectively. All transition states are validated by vibration analyses with only one imaginary frequency.

SUPPLEMENTARY MATERIALS

Supplementary material for this article is available at http://advances.sciencemag.org/cgi/content/full/6/27/eabb3831/DC1

REFERENCES AND NOTES

1. K. Weissermel, H.-J. Arpel, in *Industrial Organic Chemistry* (Wiley-VCH, 2003), pp. 59–89.
2. U. Eberle, M. Felderhoff, F. Schüth, Chemical and physical solutions for hydrogen storage. *Angew. Chem. Int. Ed.* **48**, 6608–6630 (2009).
3. R. H. Crabtree, Homogeneous transition metal catalysis of acceptorless dehydrogenative alcohol oxidation: Applications in hydrogen storage and to heterocycle synthesis. *Chem. Rev.* **117**, 9228–9246 (2017).
4. Y. Zhang, X. Cui, F. Shi, Y. Deng, Nano-gold catalysis in fine chemical synthesis. *Chem. Rev.* **112**, 2467–2505 (2012).
5. A. Sartbaeva, V. L. Kuznetsov, S. A. Wells, P. P. Edwards, Hydrogen nexus in a sustainable energy future. *Energ. Environ. Sci.* **1**, 79–85 (2008).
6. P. Jessop, Reactions with a reverse gear. *Nat. Chem.* **1**, 350–351 (2009).
7. S. Chakraborty, W. W. Brennessel, W. D. Jones, A molecular iron catalyst for the acceptorless dehydrogenation and hydrogenation of N-heterocycles. *J. Am. Chem. Soc.* **136**, 8564–8567 (2014).
8. D. Talwar, A. Gonzalez-de-Castro, H. Y. Li, J. L. Xiao, Regioselective acceptorless dehydrogenative coupling of N-heterocycles toward functionalized quinolines, phenanthrolines, and indoles. *Angew. Chem. Int. Ed.* **54**, 5223–5227 (2015).
9. W. B. Yao, Y. Zhang, X. Jia, Z. Huang, Selective catalytic transfer dehydrogenation of alkanes and heterocycles by an iridium pincer complex. *Angew. Chem. Int. Ed.* **53**, 1390–1394 (2014).
10. K. Fujita, Y. Tanaka, M. Kobayashi, R. Yamaguchi, Homogeneous perdehydrogenation and perhydrogenation of fused bicyclic N-heterocycles catalyzed by iridium complexes bearing a functional bipyridonate ligand. *J. Am. Chem. Soc.* **136**, 4829–4832 (2014).
11. R. Yamaguchi, C. Ikeda, Y. Takahashi, K.-i. Fujita, Homogeneous catalytic system for reversible dehydrogenation-hydrogenation reactions of nitrogen heterocycles with reversible interconversion of catalytic species. *J. Am. Chem. Soc.* **131**, 8410–8412 (2009).
12. A. Moores, M. Poyatos, Y. Luo, R. H. Crabtree, Catalysed low temperature H_2 release from nitrogen heterocycles. *New J. Chem.* **30**, 1675–1678 (2006).
13. A. Vivancos, M. Beller, M. Albrecht, NHC-based iridium catalysts for hydrogenation and dehydrogenation of N-heteroarenes in water under mild conditions. *ACS Catal.* **8**, 17–21 (2018).
14. S. Muthaiah, S. H. Hong, Acceptorless and base-free dehydrogenation of alcohols and amines using ruthenium-hydride complexes. *Adv. Synth. Catal.* **354**, 3045–3053 (2012).
15. K.-H. He, F.-F. Tan, C.-Z. Zhou, G.-J. Zhou, X.-L. Yang, Y. Li, Acceptorless dehydrogenation of N-heterocycles by merging visible-light photoredox catalysis and cobalt catalysis. *Angew. Chem. Int. Ed.* **56**, 3080–3084 (2017).
16. P. J. Bonitatibus Jr., S. Chakraborty, M. D. Doherty, O. Siclovan, W. D. Jones, G. L. Soloveichik, Reversible catalytic dehydrogenation of alcohols for energy storage. *Proc. Natl. Acad. Sci. U.S.A.* **112**, 1687–1692 (2015).
17. C. Deraedt, R. Ye, W. T. Ralston, F. D. Toste, G. K. Somorjai, Dendrimer-stabilized metal nanoparticles as efficient catalysts for reversible dehydrogenation/hydrogenation of N-heterocycles. *J. Am. Chem. Soc.* **139**, 18084–18092 (2017).
18. D. Forberg, T. Schwob, M. Zaheer, M. Friedrich, N. Miyajima, R. Kempe, Single-catalyst high-weight% hydrogen storage in an N-heterocycle synthesized from lignin hydrogenolysis products and ammonia. *Nat. Commun.* **7**, 13201 (2016).
19. Y. H. Han, Z. Y. Wang, R. R. Xu, W. Zhang, W. X. Chen, L. R. Zheng, J. Zhang, J. Luo, K. L. Wu, Y. Q. Zhu, C. Chen, Q. Peng, Q. Liu, P. Hu, D. S. Wang, Y. D. Li, Ordered porous nitrogen-doped carbon matrix with atomically dispersed cobalt sites as an efficient catalyst for dehydrogenation and transfer hydrogenation of N-heterocycles. *Angew. Chem. Int. Ed.* **57**, 11262–11266 (2018).
20. N. Agarwal, S. J. Freakley, R. U. McVicker, S. M. Althahban, N. Dimitratos, Q. He, D. J. Morgan, R. L. Jenkins, D. J. Willock, S. H. Taylor, C. J. Kiely, G. J. Hutchings, Aqueous Au-Pd colloids catalyze selective CH_4 oxidation to CH_3OH with O_2 under mild conditions. *Science* **358**, 223–226 (2017).
21. L. Kesavan, R. Tiruvalam, M. H. Ab Rahim, M. I. bin Saiman, D. I. Enache, R. L. Jenkins, N. Dimitratos, J. A. Lopez-Sanchez, S. H. Taylor, D. W. Knight, C. J. Kiely, G. J. Hutchings, Solvent-free oxidation of primary carbon-hydrogen bonds in toluene using Au-Pd alloy nanoparticles. *Science* **331**, 195–199 (2011).
22. S. H. Xie, H. Tsunoyama, W. Kurashige, Y. Negishi, T. Tsukuda, Enhancement in aerobic alcohol oxidation catalysis of Au_{25} clusters by single Pd atom doping. *ACS Catal.* **2**, 1519–1523 (2012).

23. N. El Kolli, L. Delannoy, C. Louis, Bimetallic Au-Pd catalysts for selective hydrogenation of butadiene: Influence of the preparation method on catalytic properties. *J. Catal.* **297**, 79–92 (2013).
24. M. Lamblin, L. Nassar-Hardy, J. C. Hierso, E. Fouquet, F. X. Felpin, Recyclable heterogeneous palladium catalysts in pure water: Sustainable developments in Suzuki, Heck, Sonogashira and Tsuji-Trost reactions. *Adv. Synth. Catal.* **352**, 33–79 (2010).
25. T. Sonobe, K. Oisaki, M. Kanai, Catalytic aerobic production of imines en route to mild, green, and concise derivatizations of amines. *Chem. Sci.* **3**, 3249–3255 (2012).
26. X. J. Cui, Y. H. Li, S. Bachmann, M. Scalone, A. E. Surkus, K. Junge, C. Topf, M. Beller, Synthesis and characterization of iron–nitrogen-doped graphene/core–shell catalysts: Efficient oxidative dehydrogenation of *N*-heterocycles. *J. Am. Chem. Soc.* **137**, 10652–10658 (2015).
27. S. M. Chen, Q. Q. Wan, A. K. Badu-Tawiah, Picomole-scale real-time photoreaction screening: Discovery of the visible-light-promoted dehydrogenation of tetrahydroquinolines under ambient conditions. *Angew. Chem. Int. Ed.* **55**, 9345–9349 (2016).
28. D. Ainembabazi, N. An, J. C. Manayil, K. Wilson, A. F. Lee, A. M. Voutchkova-Kostal, Acceptorless amine dehydrogenation and transamination using Pd-doped hydrotalcites. *ACS Catal.* **9**, 1055–1065 (2019).
29. Z.-Y. Zhai, X.-N. Guo, G.-Q. Jin, X.-Y. Guo, Visible light-induced selective photocatalytic aerobic oxidation of amines into imines on Cu/graphene. *Cat. Sci. Technol.* **5**, 4202–4207 (2015).
30. K.-N. T. Tseng, A. M. Rizzi, N. K. Szymczak, Oxidant-free conversion of primary amines to nitriles. *J. Am. Chem. Soc.* **135**, 16352–16355 (2013).
31. L. V. A. Hale, T. Malakar, K. N. T. Tseng, P. M. Zimmerman, A. Paul, N. K. Szymczak, The mechanism of acceptorless amine double dehydrogenation by *N,N,N*-amide ruthenium(II) hydrides: A combined experimental and computational study. *ACS Catal.* **6**, 4799–4813 (2016).
32. T. Mitsudome, Y. Mikami, H. Funai, T. Mizugaki, K. Jitsukawa, K. Kaneda, Oxidant-free alcohol dehydrogenation using a reusable hydrotalcite-supported silver nanoparticle catalyst. *Angew. Chem. Int. Ed.* **47**, 138–141 (2008).
33. W. E. Quinn, J. M. Baker, J. T. Latourrette, N. F. Ramsey, Radio-frequency spectra of hydrogen deuteride in strong magnetic fields. *Phys. Rev.* **112**, 1929–1940 (1958).
34. S. Kozuch, S. Shaik, How to conceptualize catalytic cycles? The energetic span model. *Acc. Chem. Res.* **44**, 101–110 (2011).
35. A. J. Medford, A. Vojvodic, J. S. Hummelshøj, J. Voss, F. Abild-Pedersen, F. Studt, T. Bligaard, A. Nilsson, J. K. Nørskov, From the Sabatier principle to a predictive theory of transition-metal heterogeneous catalysis. *J. Catal.* **328**, 36–42 (2015).
36. G. Kresse, J. Furthmüller, Efficiency of ab-initio total energy calculations for metals and semiconductors using a plane-wave basis set. *Comput. Mater. Sci.* **6**, 15–50 (1996).
37. G. Kresse, D. Joubert, From ultrasoft pseudopotentials to the projector augmented-wave method. *Phys. Rev. B.* **59**, 1758–1775 (1999).
38. S. N. Steinmann, C. Corminboeuf, Comprehensive bench marking of a density-dependent dispersion correction. *J. Chem. Theory Comput.* **7**, 3567–3577 (2011).
39. A. H. Larsen, J. J. Mortensen, J. Blomqvist, I. E. Castelli, R. Christensen, M. Dułak, J. Friis, M. N. Groves, B. Hammer, C. Hargus, E. D. Hermes, P. C. Jennings, P. B. Jensen, J. Kermode, J. R. Kitchin, E. L. Kolsbjerg, J. Kubal, K. Kaasbjerg, S. Lysgaard, J. B. Maronsson, T. Maxson, T. Olsen, L. Pastewka, A. Peterson, C. Rostgaard, J. Schiøtz, O. Schütt, M. Strange, K. S. Thygesen, T. Vegge, L. Vilhelmsen, M. Walter, Z. H. Zeng, K. W. Jacobsen, The atomic simulation environment—A Python library for working with atoms. *J. Phys. Condens. Matter* **29**, 273002 (2017).
40. G. Henkelman, B. P. Uberuaga, H. Jonsson, A climbing image nudged elastic band method for finding saddle points and minimum energy paths. *J. Chem. Phys.* **113**, 9901–9904 (2000).

Acknowledgments: We thank P. Mettraux and L. Thomas for analytical support. **Funding:** We thank the EPFL, Swiss National Science Foundation, and the Swiss Competence Center for Energy Research (SCCER) on Heat and Electricity Storage for financial support. **Author contributions:** X.C. and P.J.D. conceived and designed the experiments. X.C. performed the experiments. Z.H. contributed to TEM analysis. T.W. finished the DFT calculation. X.C., Z.F., A.P.M., T.W., and P.J.D. prepared the manuscript. All authors contributed to discussions. **Competing interests:** The authors declare that they have no competing interests. **Data and materials availability:** All data needed to evaluate the conclusions in the paper are present in the paper and/or the Supplementary Materials. Additional data related to this paper may be requested from the authors.

Submitted 20 February 2020
Accepted 15 May 2020
Published 1 July 2020
10.1126/sciadv.abb3831

Citation: X. Cui, Z. Huang, A. P. van Muyden, Z. Fei, T. Wang, P. J. Dyson, Acceptorless dehydrogenation and hydrogenation of N- and O-containing compounds on Pd_3Au_1(111) facets. *Sci. Adv.* **6**, eabb3831 (2020).